Optimised High-Order Compact Difference Schemes for Internal Acoustics Problems On Curvilinear Domains

IOP Conf. Series: Journal of Physics: Conf. Series **1184** (2019) 012005 doi:10.1088/1742-6596/1184/1/012005

Optimised High-Order Compact Difference Schemes for Internal Acoustics Problems On Curvilinear Domains

Christopher Beckwith
University of Greenwich, London, United Kingdom
E-mail: C.J.Beckwith@gre.ac.uk

Koulis Pericleous
University of Greenwich, London, United Kingdom

Valdis Bojarevics
University of Greenwich, London, United Kingdom

Abstract. A numerical framework is presented for the solution of 2D and 3D internal acoustics problems using a high-order accurate fully staggered formulation on curvilinear domains. Optimised compact finite difference schemes previously obtained in our previous paper are used for spatial discretisation, while a free parameter linear multistep method is used for temporal discretisation. The resulting scheme does not require any numerical filtering, and several benchmark cases are provided which demonstrate the significantly reduced phase velocity errors, and greater resolving efficiency compared to existing methods. Curvilinear domains are generated with the CRDT algorithm by Driscoll, with an 8th order accurate ODE solver. The governing equations for the curvilinear problem are based on a novel transformation of the decoupled velocity pressure wave equations, with simplifications made to reduce the need to interpolate derivatives at undefined locations which occur on staggered grids. The resulting transformed equations are valid only for orthogonal grids, but are computationally efficient and do not result in loss of accuracy or stability due to grid skewness. Finally, a potential application is shown, demonstrating the solution of a generated acoustic field within a crucible of liquid aluminium by a top loaded electromagnetic induction coil. Generated pressure fields agree with results shown in previous work, and demonstrate the potential use of this contactless electromagnetic excitation method as an alternative to the immersed sonotrode for the ultrasonic treatment of alloys.

1. Introduction

Implicit compact finite difference schemes have been commonly used to study various wave propagation problems [1–3]. Much of this work has focused on the optimisation and use of vertex based compact schemes. However, in a previous paper [4], the benefits of using a staggered approach were presented and demonstrated on 1D and 2D curvilinear meshes. The developed methods can be used with minimal midpoint interpolation and remain stable without numerical filtering, making them very efficient. The general formula [5] begins with the form:

$$\beta f'_{i-2} + \alpha f'_{i-1} + f'_i + \alpha f'_{i+1} + \beta f'_{i+2} = a\frac{f_{i+\frac{1}{2}} - f_{i-\frac{1}{2}}}{h} + b\frac{f_{i+\frac{3}{2}} - f_{i-\frac{3}{2}}}{3h} + c\frac{f_{i+\frac{5}{2}} - f_{i-\frac{5}{2}}}{5h} \quad (1)$$

Where α, β, a, b, c are coefficients to be determined. This staggered 6 point stencil can reach a maximum of 10^{th} order accuracy, although in practice it is often best to reduce this order to optimise the coefficients for improved wave propagation properties. In previous work [4], two methods of optimising for these coefficients were suggested. A variant of the Dispersion Relation Preserving (DRP) approach [6, 7], and a modification of the Minimised Group Velocity (MGV) approach [8–10]. A table of the obtained coefficients is given in Table 1.

Table 1: Schemes obtained using the modified DRP and MGV approaches

Scheme	a	b	c	α	β
Modified DRP 6^{th} order	.62959510	1.25602790	.10771035	.45907494	.03759173
Modified DRP 8^{th} order	.72157108	1.04449008	.06210046	.38996201	.02411880
Modified MGV 6^{th} order	.62487467	1.26524525	.11153385	.46220768	.03861920
Modified MGV 8^{th} order	.71473384	1.06149353	.06433477	.39542275	.02485832

In this paper, these optimised coefficients will be used on a number of test cases on curvilinear meshes. First, the accuracy of the method will be demonstrated with a time dependent scattering problem. Second, two new approaches of prescribing electromagnetic source terms will be presented, demonstrating their application to liquid metal processing with a top loaded induction coil. The results from the curvilinear solver will then be compared to existing work [11–13].

2. Mathematical Background

Formulations of coupled equations for wave propagation problems on curvilinear coordinates exist for non-staggered grids. Some examples include those developed in [14, 15]. Unfortunately, these are not suitable for staggered formulations as they rely on derivatives which are at undefined locations on a staggered grid. In [4], a set of continuity and momentum equations suitable for orthogonal staggered curvilinear grids were proposed, and an extension of these equations to a 2D axisymmetric system is given in equations (2)-(4). These are similar to the previously derived 2D system, but with additional terms added to the precomputed Q and R parameters to capture axisymmetric behaviour. The restriction to orthogonal coordinates prevent numerical inaccuracies and instability due to deformation which can occur on nonorthogonal meshes. While in this work these methods are not suitable for domains which have many features, such as a large duct with many obstacles, this can be overcome with the use of domain decomposition methods.

$$\frac{\partial \phi^\xi}{\partial t} = \frac{1}{\rho}\frac{\partial p}{\partial \xi}\frac{-y_\eta^2 - x_\eta^2}{(2x_\xi^2 + y_\xi^2)x_\eta^2 + x_\xi^2 y_\eta^2} + \bar{F}^\xi \quad (2)$$

$$\frac{\partial \phi^\eta}{\partial t} = \frac{1}{\rho}\frac{\partial p}{\partial \eta}\frac{-y_\xi^2 - x_\xi^2}{(2x_\eta^2 + y_\eta^2)x_\xi^2 + x_\eta^2 y_\xi^2} + \bar{F}^\eta \quad (3)$$

$$\frac{\partial p}{\partial t} = -\rho c^2 \left(\frac{\partial \phi^\xi}{\partial \xi} + \frac{\partial \phi^\eta}{\partial \eta} + Q\phi^\xi + R\phi^\eta\right) + P_s \quad (4)$$

Where:

$$Q = \frac{1}{J}(y_\eta x_{\xi\xi} - y_\xi x_{\xi\eta} - x_\eta y_{\xi\xi} + x_\xi y_{\xi\eta}) + \frac{x_\xi}{x} \tag{5}$$

$$R = \frac{1}{J}(y_\eta x_{\eta\xi} - y_\xi x_{\eta\eta} - x_\eta y_{\eta\xi} + x_\xi y_{\eta\eta}) + \frac{x_\xi}{y} \tag{6}$$

In this system, ξ and η represent the curvilinear basis vectors, ρ is the fluid density, c is the speed of sound, and F_ξ, F_η and P_s represent source terms. The mesh is assumed to have uniform spacing in the ξ and η directions, often unity for simplification in the discretised equations. The 2D system of equations can be seen as a transformation of the coupled pressure and momentum equations in Cartesian coordinates used by [11–13]. A 3D system can also be generated using the same transformation technique, and the equations for this system will be provided in Appendix A.

Curvilinear grids are generated with the CRDT algorithm by [16], using an 8^{th} order ODE solver by [17]. Initial data for the geometry is generated from a fluid simulation using in-house software SPHINX [11] and is then smoothed with the monotone piecewise cubic interpolator [18], while interpolation of internal ϕ^ξ and ϕ^η terms is handled with a compact interpolator [5]. The high-order solver ensures an accurate transformation onto the curvilinear domain, comparable to the error generated by the spatial discretisation. Spatial derivatives are calculated with the 6^{th} order modified DRP scheme in Table 1. Temporal integration is handled by the 4^{th} order 2 free parameter multistep method [19], given by equation (7) with parameters $a = 0.0108, b = -0.0069, c = 0.996, d = 0.0001477, e = 1.1245, f = -0.74$ and $g = -1.121$. These parameters give a stability boundary comparable to that of the staggered 4^{th} order Adams-Bashforth method, but with significantly reduced error. Other choices of parameters are also possible but are not used here, and an analysis of some alternatives is given in [20].

$$u(t)_i = au(t)_{i-1} + bu(t)_{i-2} + cu(t)_{i-3} + du(t)_{i-4} + dt\left(e\frac{\partial u(t)_{i-\frac{1}{2}}}{\partial t} + f\frac{\partial u(t)_{i-\frac{3}{2}}}{\partial t} + g\frac{\partial u(t)_{i-\frac{5}{2}}}{\partial t}\right) \tag{7}$$

Sound hard and sound soft boundary conditions can be implemented by assuming symmetry or antisymmetry of incoming acoustic pressure waves, respectively. In order to close the system of equations, expressions for the derivative terms on ghost nodes also need to be defined. Equations (8) and (9) describe the resulting closed system for a sound hard condition, while (8) and (10) describe a sound soft condition. The notation ϕ^j is used to denote either ϕ component as required, while i indicates the nodal position either side of the boundary, with $-i$ locations representing ghost nodes. More complex behaviour, such as impedance boundaries between two fluid elements can be modeled by including both materials in the model, and averaging the acoustic properties as shown in [21].

$$(\phi^j)_{-i} = -(\phi^j)_i \qquad (\phi^j)'_{-i} = (\phi^j)'_i \tag{8}$$

$$p_{-i} = p_i \qquad p'_{-i} = -p'_i \tag{9}$$

$$p_{-i} = -p_i \qquad p'_{-i} = p'_i \tag{10}$$

3. Electromagnetic Source Term

A contactless design [12] has previously been suggested as an alternative to the ultrasonic processing of alloy melts using a mechanical immersed sonotrode. As this approach is contactless, it can be used for high temperature melts, or on highly reactive alloys such as gamma-TiAl in which a traditional sonotrode would corrode and risk the contamination of the metal. However, unlike the traditional approach, the induced acoustic pressure from the coil is not enough to

reach the approximated 0.7MPa cavitation threshold [22], with a 0.1T AC coil operating at 20kHz only generating acoustic pressures of approximately 2000Pa in aluminium. The electromagnetic source term induced by the top coil is derived from the Lorentz force $\mathbf{F} = \mathbf{J} \times \mathbf{B}$ which has a mean component driving bulk mixing of the fluid, and a time dependent component which induces periodic compression waves perpendicular to the surface of the fluid. The induced forces deform the top surface, resulting in a geometry which is more suitable for a curvilinear solver. A three turn copper coil is used, which is lowered to be in close proximity to the computed top surface [12], and operates with an induced AC current of 1700A, creating a magnetic field of approximately 0.1T. The magnetic permeability of the liquid is assumed to be approximately $0.8\mu_0$ in liquid aluminium. Where $\mu_0 = 4\pi \times 10^{-7}\mathrm{H\,m^{-1}}$ is the permeability of free space. The electrical conductivity σ of the fluid can be calculated following measurements by [23], and is approximately 3×10^6 at the melting point of $660.32°C$, with a density of $2375\mathrm{kg\,m^{-3}}$. For a coil operating at 10kHz, these measurements result in a skin layer depth of approximately 2.9mm.

Previously, a stepwise approach for the sloped crucible walls has been used by [12, 13] with promising results. However, the stepwise approach has two main drawbacks. First, the steep incline of the walls of the crucible are not fully captured unless the computational domain consists of many more points than are needed to capture the acoustic wave, and second, the reflections off such walls are not reflected at a small angle, which could build up error over long simulations. Instead, the new curvilinear compact difference solver that has been developed could be employed to capture these angled reflections accurately while minimising the required number of grid points.

$$\tilde{\mathbf{F}} = \frac{1}{\sqrt{2}\mu\delta} B_0^2 \exp^{2\frac{S_d}{\delta}} \left[\sqrt{2}\cos(2\omega t - 2\frac{S_d}{\delta} + \frac{\pi}{4})\right] \tag{11}$$

In previous studies, the force term has been treated directly as the momentum source term (11), with the time dependent part of the Lorentz force $\tilde{\mathbf{F}}$ operating normal to the surface, and S_d representing the euclidean distance to the surface. However, for a staggered system, this approach is only appropriate for cases where the boundaries can be assumed to be sound-soft. The strength of the Lorentz force decays rapidly within the skin layer, with a 90% reduction in amplitude by 1.5δ. As a result, it is important to use a source term defined close to the domain boundary, which for a staggered system could be either momentum or pressure depending on boundary conditions. Not treating the source term this way would result in significant source term errors and overall reduced pressure magnitudes. If the boundaries are sound-soft, the source terms for this system in the curvilinear vector space can be represented with equations (12)-(13).

$$\bar{F}^{\xi} = \frac{\left(\xi_x \tilde{\mathbf{F}}_x + \xi_y \tilde{\mathbf{F}}_y\right)}{h_\xi} \tag{12}$$

$$\bar{F}^{\eta} = \frac{\left(\eta_x \tilde{\mathbf{F}}_x + \eta_y \tilde{\mathbf{F}}_y\right)}{h_\eta} \tag{13}$$

Where $h_\eta = \sqrt{\left(\frac{\partial x}{\partial \eta}\right)^2 + \left(\frac{\partial y}{\partial \eta}\right)^2}$ and $h_\xi = \sqrt{\left(\frac{\partial x}{\partial \xi}\right)^2 + \left(\frac{\partial y}{\partial \xi}\right)^2}$. However, if we assume the Lorentz force acts normally to the deformed surface then locally the contribution to the force in the direction perpendicular to the surface is zero. Choosing η as the coordinate line along the top edge, $\bar{F}^{\eta} = 0$ and $\bar{F}^{\xi}$ is given in equation (14).

$$\tilde{\mathrm{F}}^{\xi} = \frac{1}{\sqrt{2}h_\xi\mu\delta} B_0^2 \exp^{2\frac{S_d}{\delta}} \left[\sqrt{2}\cos(2\omega t - 2\frac{S_d}{\delta} + \frac{\pi}{4})\right] \tag{14}$$

For a sound-hard boundary, represented by a zero normal velocity condition, it is instead preferable to treat the Lorentz force as a pressure source term. Thus, $\bar{F}^{\xi} = \bar{F}^{\eta} = 0$ and the derived pressure source is given in (15).

$$P_s = -W(t,a,b,n)c^2\frac{B^2\sqrt{2}}{2\delta^2\mu\,\omega}\exp^{-2\frac{S_d}{\delta}}\left(\cos\left(2\omega t - 2\frac{S_d}{\delta} + \frac{\pi}{4}\right) + \sin\left(2\omega t - 2\frac{S_d}{\delta} + \frac{\pi}{4}\right)\right) \quad (15)$$

In this equation, W represents a smoothing function introduced to prevent spurious shockwaves due to instantaneous pressures within the skin layer over the first few time steps. This allows the numerical scheme to retain a high degree of accuracy, and the chosen function is given in (16). Where a, b, and n are coefficients to be chosen. The time difference $b-a$ should be large enough such that the ramp is allowed to smooth the source over multiple time steps, but is small enough to remain significantly smaller than the period of oscillation.

$$W(t;a,b,n) = \begin{cases} 0 & \text{if } t \le a \\ \left(\frac{x-a}{b-a}\right)^n \sum_{j=0}^{n-1}\binom{n+j-1}{j}\left(\frac{b-x}{b-a}\right)^j & \text{if } a < t < b \\ 1 & \text{if } t \ge b \end{cases} \quad (16)$$

4. Simulation Results

4.1. Flow around a Cylinder

To first verify the curvilinear equations and obtained compact schemes without the presence of an electromagnetic field, the scattering from an infinite cylinder is modelled, matching the benchmark problem [24]. The cylinder has a non-dimensionalised radius $r = 0.5$, and the outer edge of the domain is taken to be at $r = 15$. Non-reflecting boundary conditions are used along the outside edge. The initial conditions are $\phi^{\xi} = \phi^{\eta} = 0$ and

$$p(r,\theta,0) = \exp\left[-\frac{5}{2}\ln(2)(r^2 - 8r\cos\theta + 16)\right] \quad (17)$$

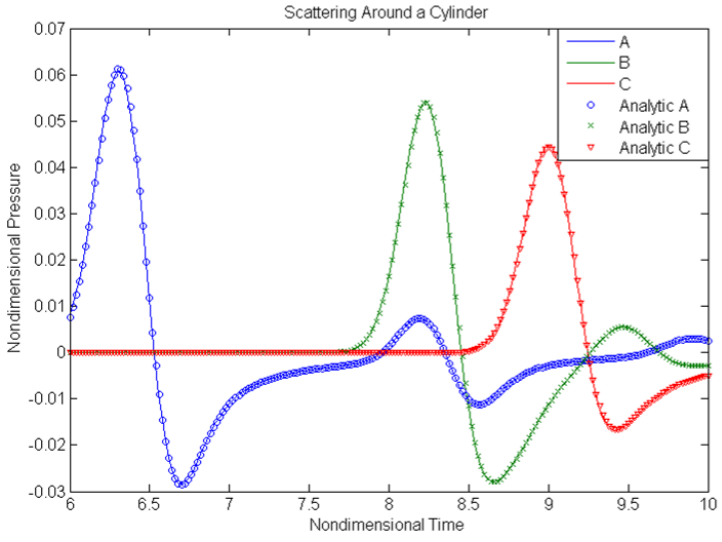

Figure 1: Pressure field at nodal locations A, B, and C.

The pressure field is calculated up to a non-dimensionalised time $t = 10$ at three points $A(r = 5, \theta = \pi/2)$, $B(r = 5, \theta = 3\pi/4)$, and $C(r = 5, \theta = \pi)$. An O-Grid is used for computation, and only the top half of the circular domain is modelled, with a symmetry boundary at $\theta = 0$ and $\theta = \pi$. 160 grid points are used in the azimuthal direction, and 223 gridpoints in the radial direction. This results in approximately 4.55 points per wavelength (PPW) in the radial direction, approximately 50 PPW in the azimuthal direction around the cylinder, and 6.34 PPW near the source at $r = 4$. The system remains above the Nyquist limit up to $r = 12.7$, with 1.99 PPW. The grid achieves a required 0.01 error tolerance for all $r < 8$. A timestep size $\Delta t = 0.002$ is used, slightly lower than the stability limit for this system.

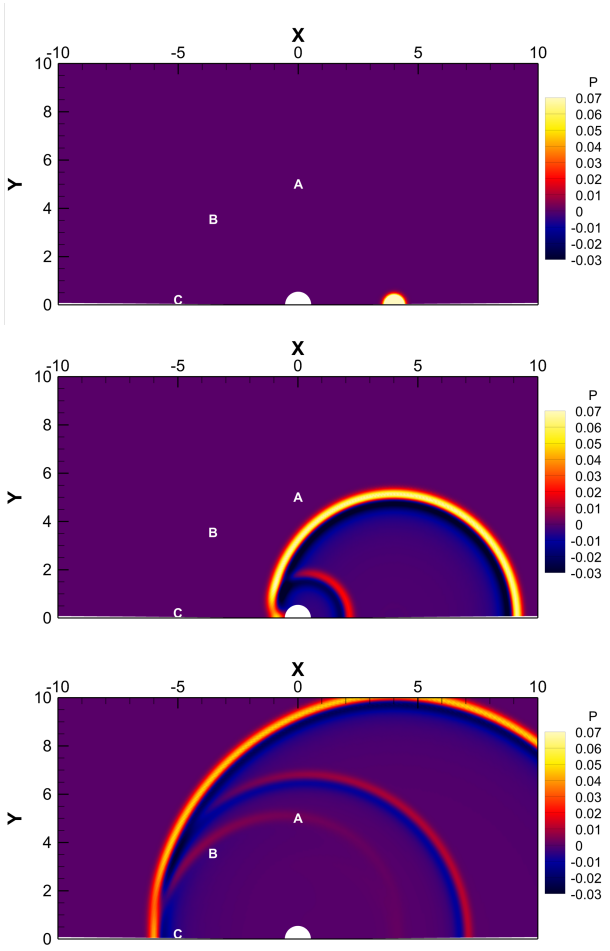

Figure 2: Pressure field at $t = 0, 5, 10$.

The solution at all nodal points agree well with the reference solution. Figure 1 shows the pressure history from $t = 6$ to $t = 10$ at intervals of 0.02. The pressure distributions at $t = 0$, 5, and 10 are given in 2. Peak pressures at each node are reached at approximately 6.3, 8.2 and 9.0 respectively. L_2 norms are taken over this time interval, and the errors at all nodes remain under 1×10^{-2}, with the largest error recorded at node A, with an error of approximately 5×10^{-2}.

4.2. Electromagnetically Induced Sound In A Crucible

A body of liquid aluminium is excited by a coil operating at a range of frequencies between 8.8 and 8.9kHz, resulting in an acoustic oscillation between 17.6 and 17.8kHz. A microphone

placed 70cm above the top surface of the liquid recorded the acoustic signal, and a spectrogram of the signal is given in Figure 3. The experiment was carried out by partners involved in the ExoMet project (FP7-NMP3-LA-2012-280421) and the spectrogram produced in Adobe Audition. Broadband noise is detected which could signal the existence of cavitation within the crucible. This should only be obtainable through acoustic resonance as the ±2000Pa induced pressure from the initial acoustic source is not enough to trigger cavitation alone.

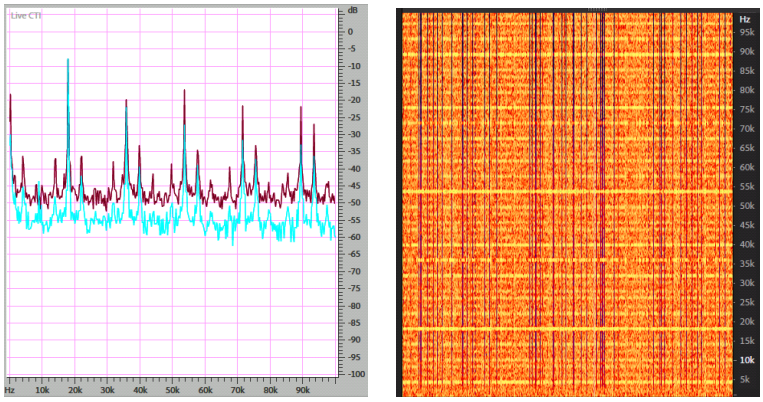

Figure 3: FFT spectrum (left) and spectrogram (right) show broadband noise when excited between 8.8 and 8.9kHz, a sign of cavitation occurring in the crucible.

Performing an eigenfrequency study in COMSOL, we can see that a resonant mode close to the 17.8kHz range is only expected if the top boundary were to act as a hard surface, which would result in a fundamental frequency of around 18295Hz. While the numerical frequency is 2.78% higher than the experimental frequency, this is close enough that we would expect to see significant resonant "beats" in the experiment.

Table 2: Resonant frequencies (Hz) generated from a COMSOL 3D eigenfrequency study

Free Surface (Sound Soft)	Hard Surface (Sound Hard)
13272	18295
29759	19404
29760	30543
33882	30544
43173	31156
43957	32113

A list of the first 6 eigenfrequencies for this model are given in Table 2. It is possible that this experimental result is due to acoustic reflections from a thick oxide layer along the interface in the small crucible, as other experiments with larger crucibles have shown the top surface to be represented well as a sound soft boundary. To calculate the value of B_0 along the top surface, a frequency domain study is performed using the COMSOL AC/DC package, at half the obtained acoustic resonant frequencies. The magnetic field strength is extracted along the interface between the air and liquid aluminium. The results for a coil operating at 9147.5Hz are

given in Figure 4, and show a steep increase in the magnetic field strength near $r = 0.4$m, where the coil is closest to the liquid. The shape of this curve, and the strength of the Lorentz force induced in the fluid, is very sensitive to the position of the coil relative to the surface. In this work, the position has been matched to available images of physical experiments as closely as possible. However in future work, obtaining the geometry through an accurate numerical MHD simulation would be preferred.

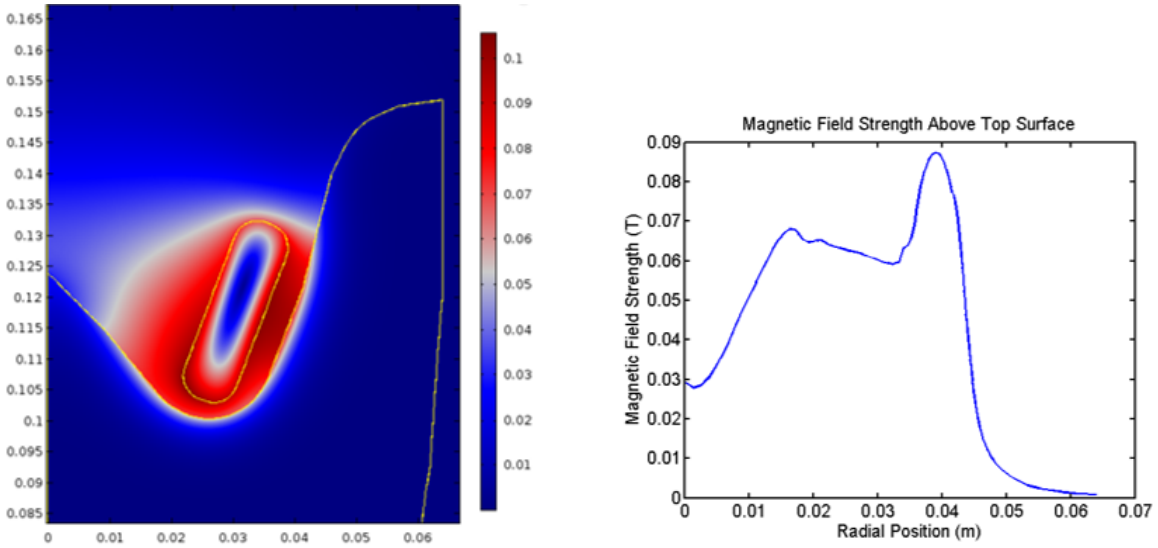

(a) Magnetic Flux Density above top surface (b) Magnetic Flux Density along the top surface

Figure 4: Magnetic Flux Density induced by the induction coil operating at 9147.5Hz (left), and resulting field strength along the top surface B_0 (right).

The computed acoustic eigenfrequencies are then used to drive the time dependent study using the newly obtained 6th order Modified DRP scheme.

4.2.1. Sound Hard Top Surface Following from experiments, which seem to suggest the top surface is acting similarly to a sound hard boundary, curvilinear equations (2)-(4) are used along with a source term given by equation (14). A staggered curvilinear grid is generated with the CRDT algorithm and the overlapping grids are shown in Figure 5.

The results of the sound hard study are given in the previous work [4]. The initial reflections off the boundary walls were noted to be around $t \approx 1.6 \times 10^{-5}s$, and by $t \approx 7.6 \times 10^{-4}$s the resonant eigenmode is noticeable, agreeing with the result from the COMSOL eigenfrequency study. The maximum induced pressure from the coil is approximately 1800Pa, which agrees with previous studies [12, 13]. While this is not enough to trigger cavitation, the sustained resonance should allow pressures to build up to the required threshold of approximately 200kPa. At which point the eigenfrequency solution would break down due to locally variant speed of sound and source terms with secondary frequencies produced by the collapsing bubble. This study served as a validation of the method for the linear regime, and the accuracy of the method should also be benefitial when introducing additional terms to handle the non-linear cavitating regime, but this is yet to be tested.

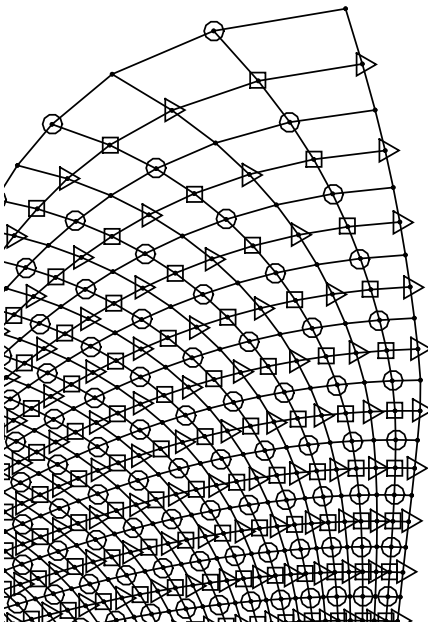

Figure 5: The curvilinear representation of the crucible with staggered grids (a), with pressure nodes (squares) located at the cell centoids, and velocity nodes ϕ^{η} (triangles) and ϕ^{ξ} (circles) on cell edges.

4.2.2. Sound Soft Top Surface However, in previous studies a sound soft top surface was assumed with similar peak pressures of approximately 2000Pa. To validate the derived source term in equation (14), the previous study is repeated using a zero pressure top surface. The induction coil is then set to operate at 16941kHz, causing acoustic excitation at the expected 33882kHz. The magnetic field strength distribution given in Figure 4 remains unchanged, due to the coil operating at the same power and the shape of the top surface remaining constant. Snapshots of the induced force in the liquid aluminium over one time period can be seen in Figure 6. The results from using the 6^{th} order modified DRP scheme show sustained resonance, and do not trigger near-resonant beats in the 18 cycle simulation. Initial wave reflections off the boundary walls can be seen at around $t \approx 1.64 \times 10^{-5}$s, and by $t \approx 2.6 \times 10^{-4}$s the resonant eigenmode is noticeable, although it does not fully form until much later as seen in Figure 7f. The pressure distribution agrees well with the mode obtained from a COMSOL eigenfrequency study.

An initial pressure contribution of approximately 1700Pa can also be noted, only slightly lower than the roughly 1800Pa contribution in the sound hard case study, and the record pressures of around 2000Pa in previous work. This small reduction is due to a peak magnetic field strength of 0.09T in the eigenfrequency study, while the previous work assumed a uniform magnetic field of 0.1T. Resonance is particularly noticeable by point C in Figure 8, which shows the time evolution of the pressure at a point on the outside wall A($x = 0.05855$m,y $= 0.06946$m), and at the lowest point B ($x = 0$m,$y = 0$m), and just under the boundary closest to the coil C ($x = 0.0418916$m,$y = 0.111534$m). The position of the sensors can be seen in Figure 7a.

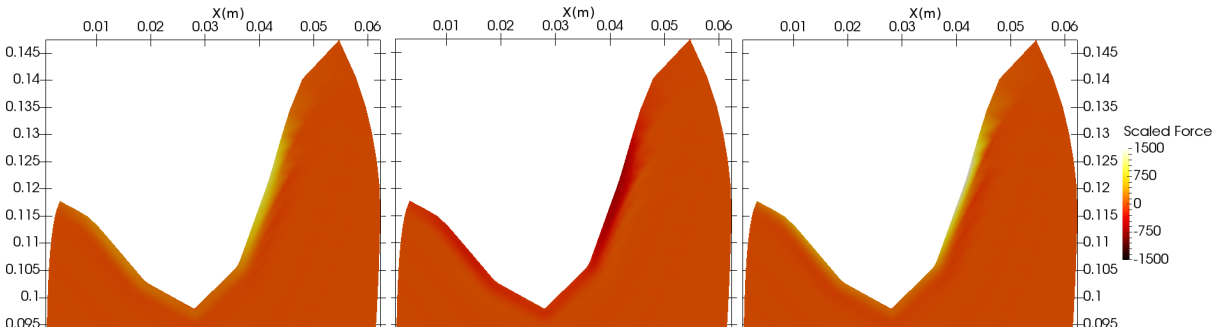

(a) $t \approx 0s$ (b) $t \approx 1.8 \times 10^{-5}s$ (c) $t \approx 3 \times 10^{-5}s$

Figure 6: Scaled Lorentz force distribution along the top surface, over one acoustic period.

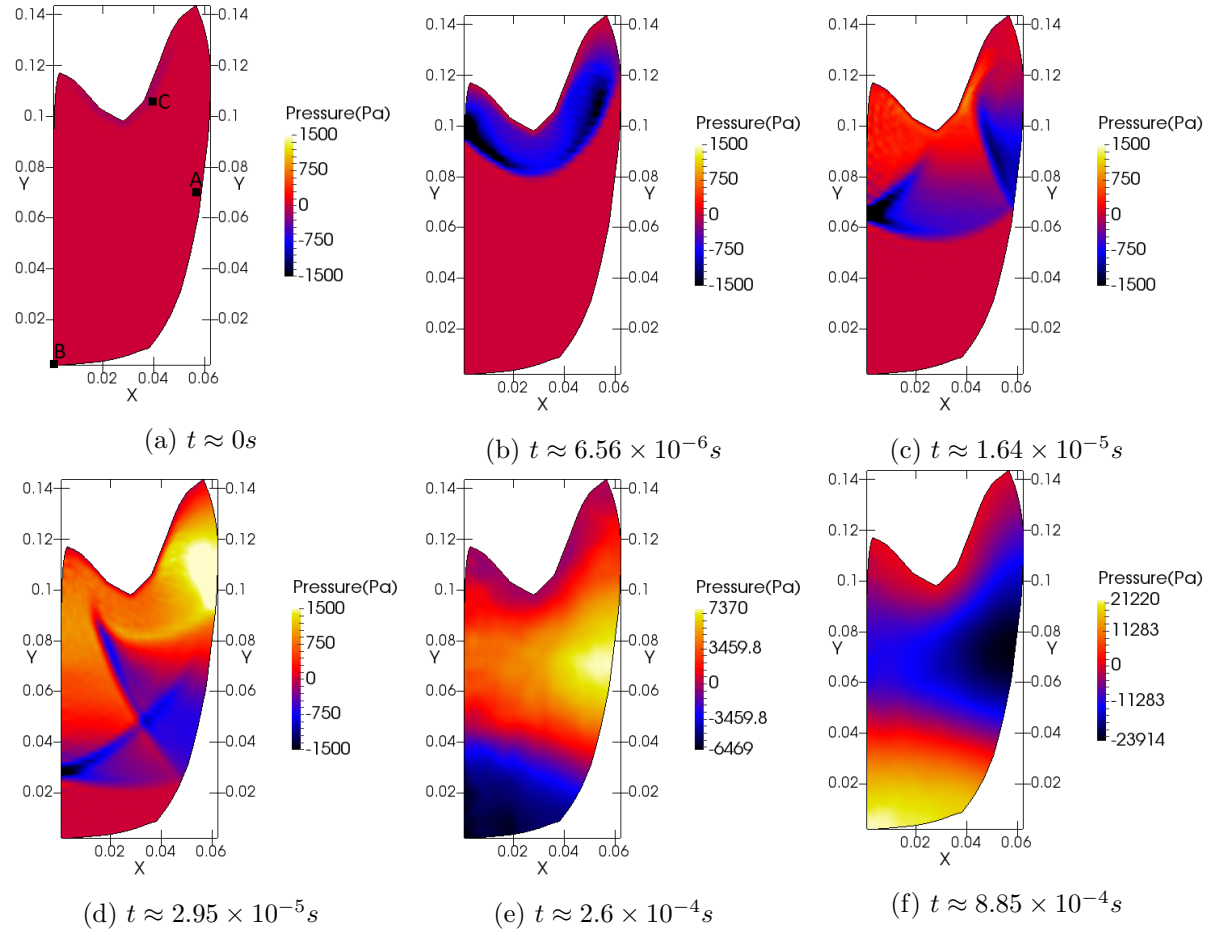

(a) $t \approx 0s$ (b) $t \approx 6.56 \times 10^{-6}s$ (c) $t \approx 1.64 \times 10^{-5}s$

(d) $t \approx 2.95 \times 10^{-5}s$ (e) $t \approx 2.6 \times 10^{-4}s$ (f) $t \approx 8.85 \times 10^{-4}s$

Figure 7: Pressure time evolution in a crucible with a free surface. Forcing frequency 33882Hz.

It can be noted that the new pressure source term, the scaled momentum source, and the existing treatment used by [12, 25] all yield similar results, serving as a good validation of the source term treatment. We can also see that the existence of a thick aluminium oxide layer does not appear to significantly influence the pressure contribution caused by the induced field as long as the distance between the coil and the liquid aluminium is unchanged. This is expected, as aluminium oxide is not a suitably conducting material.

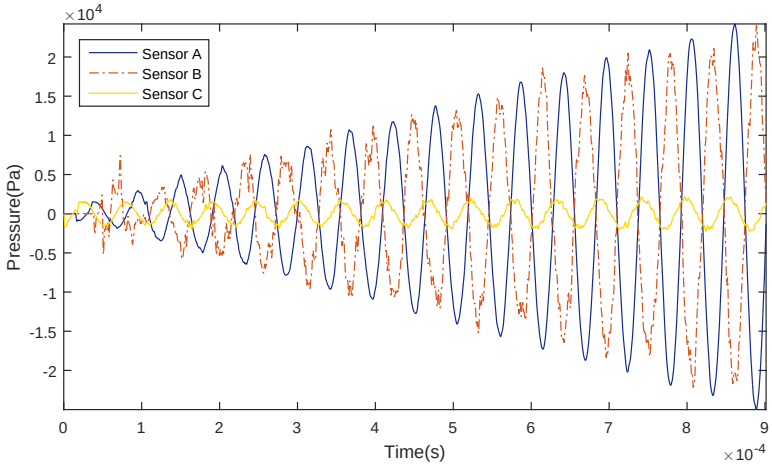

Figure 8: Pressure time evolution at sensors A(0.05855m,0.06946m), B(0m,0m), and C(0.0418916m,0.111534m). Forcing frequency 33882Hz.

5. Conclusions and Future Work

This paper has demonstrated the application of high-order staggered compact schemes on curvilinear domains to simulations involving source terms generated through EM induction. The combination of high-order numerical discretisation, midpoint interpolation, and grid generation results in highly accurate simulations which are more efficient than other methods currently being used in the field, which often require numerical filtering to remain stable. These methods were first tested on a simple benchmark problem, and the results match well against analytic solutions. Initial work applied to a crucible of liquid aluminium is also presented, which reproduce similar pressure readings to existing work [12, 25] in the laminar regime. As a topic for future work, additional coupling to correctly model the unstable cavitating regime is required for practical use in liquid metal processing applications.

Appendix A. Full 3D Curvilinear Coupled Equations

The 2D axisymmetric system used in this paper is derived from a simplification of the full 3D system. The momentum equations (18)-(20) and pressure equation (21) describe the propagation of a wave in full 3D space.

$$\frac{\partial \phi^{\xi}}{\partial t} = \frac{1}{\rho J^2}\frac{\partial p}{\partial \xi}((2x_\eta^2 + y_\eta^2 + z_\eta^2)x_\zeta^2 + 2x_\eta x_\zeta y_\eta y_\zeta + (x_\eta^2 + 2y_\eta^2 + z_\eta^2)y_\zeta^2 + z_\zeta^2(x_\eta^2 + y_\eta^2)) \tag{18}$$

$$\frac{\partial \phi^{\eta}}{\partial t} = \frac{1}{\rho J^2}\frac{\partial p}{\partial \eta}((2x_\xi^2 + y_\xi^2 + z_\xi^2)x_\zeta^2 + 2x_\xi x_\zeta y_\xi y_\zeta + (x_\xi^2 + 2y_\xi^2 + z_\xi^2)y_\zeta^2 + z_\zeta^2(x_\xi^2 + y_\xi^2)) \tag{19}$$

$$\frac{\partial \phi^{\zeta}}{\partial t} = \frac{1}{\rho J^2}\frac{\partial p}{\partial \zeta}((2x_\xi^2 + y_\xi^2 + z_\xi^2)x_\eta^2 + 2x_\xi y_\xi x_\eta y_\eta + (x_\xi^2 + 2y_\xi^2 + z_\xi^2)y_\eta^2 + z_\eta^2(x_\xi^2 + y_\xi^2)) \tag{20}$$

$$\frac{\partial p}{\partial t} = -\rho c^2\left(\frac{\partial \phi^{\xi}}{\partial \xi} + \frac{\partial \phi^{\eta}}{\partial \eta} + \frac{\partial \phi^{\zeta}}{\partial \zeta} + \frac{1}{J}\left(Q\phi^{\xi} + R\phi^{\eta} + S\phi^{\zeta}\right)\right) \tag{21}$$

Where the coefficients Q, R, and S can be precomputed and have expressions:

$$\begin{aligned} Q =& (y_\eta z_\zeta - z_\eta y_\zeta)x_{\xi\xi} - (y_\xi z_\zeta - z_\xi y_\zeta)x_{\xi\eta} + (y_\xi z_\eta - z_\xi y_\eta)x_{\xi\zeta} \\ & - (x_\eta z_\zeta - z_\eta x_\zeta)y_{\xi\xi} + (x_\xi z_\zeta - z_\xi x_\zeta)y_{\xi\eta} - (x_\xi z_\eta - z_\xi x_\eta)y_{\xi\zeta} \\ & (x_\eta y_\zeta - y_\eta x_\zeta)z_{\xi\xi} - (x_\xi y_\zeta - y_\xi x_\zeta)z_{\xi\eta} + (x_\xi y_\eta - y_\xi x_\eta)z_{\xi\zeta} \end{aligned} \tag{22}$$

$$\begin{aligned} R =&(y_\eta z_\zeta - z_\eta y_\zeta)x_{\eta\xi} - (y_\xi z_\zeta - z_\xi y_\zeta)x_{\eta\eta} + (y_\xi z_\eta - z_\xi y_\eta)x_{\eta\zeta} \\ &- (x_\eta z_\zeta - z_\eta x_\zeta)y_{\eta\xi} + (x_\xi z_\zeta - z_\xi x_\zeta)y_{\eta\eta} - (x_\xi z_\eta - z_\xi x_\eta)y_{\eta\zeta} \\ &(x_\eta y_\zeta - y_\eta x_\zeta)z_{\eta\xi} - (x_\xi y_\zeta - y_\xi x_\zeta)z_{\eta\eta} + (x_\xi y_\eta - y_\xi x_\eta)z_{\eta\zeta} \end{aligned} \tag{23}$$

$$\begin{aligned} S =&(y_\eta z_\zeta - z_\eta y_\zeta)x_{\zeta\xi} - (y_\xi z_\zeta - z_\xi y_\zeta)x_{\zeta\eta} + (y_\xi z_\eta - z_\xi y_\eta)x_{\zeta\zeta} \\ &- (x_\eta z_\zeta - z_\eta x_\zeta)y_{\zeta\xi} + (x_\xi z_\zeta - z_\xi x_\zeta)y_{\zeta\eta} - (x_\xi z_\eta - z_\xi x_\eta)y_{\zeta\zeta} \\ &(x_\eta y_\zeta - y_\eta x_\zeta)z_{\zeta\xi} - (x_\xi y_\zeta - y_\xi x_\zeta)z_{\zeta\eta} + (x_\xi y_\eta - y_\xi x_\eta)z_{\zeta\zeta} \end{aligned} \tag{24}$$

References

[1] Kim J W and Lee D J 1996 *AIAA journal* **34** 887–893
[2] Kim J W 2007 *Journal of Computational Physics* **225** 995–1019
[3] Liu Z, Huang Q, Zhao Z and Yuan J 2008 *International journal of aeroacoustics* **7** 123–146
[4] Beckwith C, Pericleous K and Bojarevics V 2017 Development and application of optimised compact difference schemes to linear acoustics problems in orthogonal curvilinear coordinates *ICSV24*
[5] Lele S K 1992 *Journal of computational physics* **103** 16–42
[6] Tam C K and Webb J C 1993 *Journal of computational physics* **107** 262–281
[7] Bogey C and Bailly C 2004 *Journal of Computational physics* **194** 194–214
[8] Holberg O 1987 *Geophysical prospecting* **35** 629–655
[9] Venutelli M 2011 *International Journal of Computational Fluid Dynamics* **25** 287–296
[10] Venutelli M 2015 *Applied Numerical Mathematics* **87** 53–73
[11] Bojarevics V, Roy A A and Pericleous K 2010 *Magnetohydrodynamics* **46** 317–329
[12] Bojarevics V, Djambazov G S and Pericleous K A 2015 *Metallurgical and Materials Transactions A* **46** 2884–2892
[13] Djambazov G, Bojarevics V, Lebon B and Pericleous K 2014 Contactless acoustic wave generation in a melt by electromagnetic induction *Light Metals 2014* (Springer) pp 1379–1382
[14] Ghillani P 2013 *Aeroacoustic simulation of a linear cascade by a prefactored compact scheme* Ph.D. thesis University of Leicester
[15] Abrahamsson L and Kreiss H O 1994 *Journal of Computational Physics* **111** 1–14
[16] Driscoll T A and Vavasis S A 1998 *SIAM Journal on Scientific Computing* **19** 1783–1803
[17] Dormand J R and Prince P J 1980 *Journal of computational and applied mathematics* **6** 19–26
[18] Fritsch F N and Carlson R E 1980 *SIAM Journal on Numerical Analysis* **17** 238–246
[19] Ghrist M, Fornberg B and Driscoll T A 2000 *SIAM Journal on Numerical Analysis* **38** 718–741
[20] Ghrist M L 2000 *High-order finite difference methods for wave equations* Ph.D. thesis University of Colorado
[21] Moczo P, Kristek J, Vavrycuk V, Archuleta R J and Halada L 2002 *Bulletin of the Seismological Society of America* **92** 3042–3066
[22] Tzanakis I, Lebon G, Eskin D and Pericleous K 2017 *Ultrasonics sonochemistry* **34** 651–662
[23] Apfel'baum E M 2003 *High temperature* **41** 466–471
[24] Tam C K and Hardin J C 1997 Second computational aeroacoustics (caa) workshop on benchmark problems
[25] Djambazov G, Bojarevics V, Shevchenko D, Burnard D, Griffiths W and Pericleous K 2017 Sensitivity of contactless ultrasound processing to variations of the free surface of the melt with induction heating *8th International Symposium on High-Temperature Metallurgical Processing* (Springer) pp 289–298